Bridging the gap between presynaptic hair cell function and neural sound encoding

Lina María Jaime Tobón[1,2,3,4,*] & Tobias Moser[1,2,3,4,*]

[1]Auditory Neuroscience and Synaptic Nanophysiology Group, Max Planck Institute for Multidisciplinary Sciences, Göttingen, Germany; [2]Institute for Auditory Neuroscience, University Medical Center Göttingen, Göttingen, Germany; [3]Collaborative Research Center 889, University of Göttingen, Göttingen, Germany; [4]Multiscale Bioimaging of Excitable Cells, Cluster of Excellence, 37075 Göttingen, Germany

*Paste corresponding author name(s) here: Lina María Jaime Tobón, Tobias Moser
Email: ljaimet@mpinat.mpg.de, tmoser@gwdg.de

Author Contributions: TM and LMJT designed the study. LMJT performed the experiments and the analysis. TM and LMJT prepared the manuscript.

Competing Interest Statement: The authors declare that no competing interests exist.

Classification: Biological Sciences: Neuroscience.

Keywords: paired recordings, synaptic heterogeneity, sound intensity coding, active zone, synaptic vesicle

This PDF file includes:

Main Text
Figures 1 to 4

Abstract

Neural diversity can expand the encoding capacity of a circuitry. A striking example of diverse structure and function is presented by the afferent synapses between inner hair cells (IHCs) and spiral ganglion neurons (SGNs) in the cochlea. Synapses at the pillar IHC-side activate at lower voltages than those of the modiolar side, which show larger active zones and Ca^{2+}-channel clusters. At the postsynapse, SGNs differ in their spontaneous firing rates, sound thresholds and operating ranges. While it is tempting to speculate about a causal relationship between synaptic heterogeneity and neural response diversity, direct experimental evidence is lacking. Here, we bridged this gap by *ex-vivo* paired recordings of IHCs and postsynaptic boutons with stimuli and conditions aimed to mimic those of *in-vivo* SGN-characterization. Synapses with high spontaneous

rate (*SR*) were found predominantly on the pillar side of the IHC. These high *SR* synapses had larger spontaneous EPSCs, lower voltage-thresholds, shorter response latencies and higher initial release rates. This study indicates that synaptic heterogeneity in IHCs can account for functional response diversity of spontaneous and sound-evoked SGN.

Significance Statement

Sound encoding relies on spiral ganglion neurons (SGNs) with diverse spontaneous activities, sound thresholds and sound intensity ranges over which firing rates change. Such functional SGN diversity might originate from different input provided by the presynaptic inner hair cells (IHCs) at their afferent synapses. The present study addresses this hypothesis by using recordings from individual IHC-SGN synapses. The results provide evidence that synaptic heterogeneity in IHCs underlies SGN firing diversity. Thus, IHCs seem to employ diverse active zones to decompose sound information into different neural pathways that collectively inform the brain.

Introduction

Chemical synapses represent diverse and plastic neural contacts that are adapted to the specific needs of neural computation. Such diversity is expressed across the nervous system, within a given circuit and even within the same neuron (recent reviews in Ref. Nusser, 2018; Wichmann & Kuner, 2022). Synaptic diversity occurs at various levels: from synapse shape and size, to the ultrastructure of pre- and postsynaptic specializations, to their molecular composition. The auditory system harbors exciting examples of synaptic heterogeneity. Glutamatergic ribbon synapses in the cochlea, calyceal synapses in the brainstem, and bouton synapses throughout the central auditory system differ greatly from each other (Moser et al., 2006; Wichmann & Kuner, 2022). Beyond the complexity across synapses formed by different neurons, heterogeneity exists even among auditory synapses of an individual presynaptic inner hair cell (IHC) with its 5-30 postsynaptic spiral ganglion neurons (SGNs, (reviews in: Meyer & Moser, 2010; Moser, 2020; Reijntjes & Pyott, 2016)). Such synaptic heterogeneity is a candidate mechanism by which the cochlea decomposes acoustic information (Gómez-Casati & Goutman, 2021). IHCs might use such heterogeneous synapses to

break down sound intensity information into complementary spike rate codes that result in diverse firing properties of SGNs that have been reported across species (Huet et al., 2016; Kiang et al., 1965; Sachs & Abbas, 1974; Taberner & Liberman, 2005; Winter et al., 1990).

Decades of *in vivo* recordings from single SGNs have demonstrated the functional diversity of SGNs at a given tonotopic place. This functional diversity is present in both spontaneous and sound-evoked firing. The spontaneous firing rate (SR) in the absence of sound varies from less than 1 spikes/s to more than 100 spikes/s (Barbary, 1991; Evans, 1972; Kiang et al., 1965; Schmiedt, 1989; Taberner & Liberman, 2005). In response to increasing sound pressure, SGNs with high SR show a low sound threshold and a steep rise in the spike rate to increasing sound intensities until the rate saturates. SGNs with low SR have a higher sound thresholds, shallower spike rate rise and saturate at higher sound intensities (Ohlemiller et al., 1991; Winter et al., 1990). Additionally, SGNs show differences in their excitability (Crozier & Davis, 2014; Markowitz & Kalluri, 2020; Smith et al., 2015), morphological features (M. C. Liberman, 1980; Merchan-Perez & Liberman, 1996; Tsuji & Liberman, 1997) and heterogeneous molecular profiles (C. Li et al., 2020; Petitpré et al., 2018, 2020; Shrestha et al., 2018; Sun et al., 2018). Yet, it has remained challenging to demonstrate a causal link of a candidate mechanism to the physiological SGN diversity.

One common approach has been to capitalize on a pioneering study employing *in vivo* labelling of physiologically characterized SGNs in cats proposing that synapses formed by low and high SR SGNs segregate on the basal IHC pole (M. C. Liberman, 1982). High SR SGNs preferentially contacted the pillar side of the IHC (facing pillar cells), while low SR SGNs synapsed on the opposite, modiolar side of the IHC (facing the cochlear modiolus). Interestingly, a segregation has also been found for afferent and efferent synaptic properties, as well as molecular and biophysical SGN properties (Frank et al., 2009; Grant et al., 2010; Hua et al., 2021; Kantardzhieva et al., 2013; L. D. Liberman et al., 2011; Markowitz & Kalluri, 2020; Merchan-Perez & Liberman, 1996; Meyer et al., 2009; Neef et al., 2018; Ohn et al., 2016; Özçete & Moser, 2020; Shrestha et al., 2018; Sun et al., 2018; Yin et al., 2014). For instance, pillar IHC active zones (AZs) have smaller ribbons (L. D. Liberman et al., 2011; Ohn et al., 2016; Reijntjes et al., 2020), and activate at voltages as low

as the IHC resting potential (Ohn et al., 2016; Özçete & Moser, 2020). Does the functional SGN diversity arise from such synaptic heterogeneity? The ensuing presynaptic hypothesis states that the low voltage activation of pillar AZs mediates the high SR and low sound threshold of their postsynaptic SGNs. However, evidence linking topographical synaptic position, AZ function and postsynaptic SGN response remains to be provided.

Here, we aimed to bridge the gap between *ex vivo* presynaptic physiology and *in vivo* SGN neurophysiology to study the diversity of IHC-SGNs synapses. We performed paired IHC and SGN bouton recordings in acutely explanted organs of Corti from hearing mice with stimuli and conditions aimed to mimic *in vivo* SGN-characterization. This tightly controls IHC Ca^{2+} influx and records the postsynaptic response to glutamate release from a single synapse. Using the rate of spontaneous excitatory postsynaptic currents (rate of sEPSCs, *SR*) as a surrogate for SGN SR, we demonstrate that high *SR* synapses have larger and more compact sEPSCs, as well as lower voltage thresholds, shorter latencies of evoked EPSCs and higher initial release rates. About 89% of these high *SR* synapses were located on the pillar side of the IHC. Our findings indicate that synaptic heterogeneity of IHCs explains much of the SGN firing diversity.

Results

In the present study, we analyzed synaptic transmission at individual afferent IHC-SGN synapses of mice after the onset of hearing. We aimed to mimic physiological conditions as closely as possible during our *ex vivo* experiments. We combined perforated-patch whole-cell recordings from IHCs, held at their presumed physiological resting potential, with ruptured-patch whole-cell

recordings from one of the postsynaptic SGN boutons (Fig. 1) at body temperature and in artificial perilymph-like solution (Wangemann & Schacht, 1996).

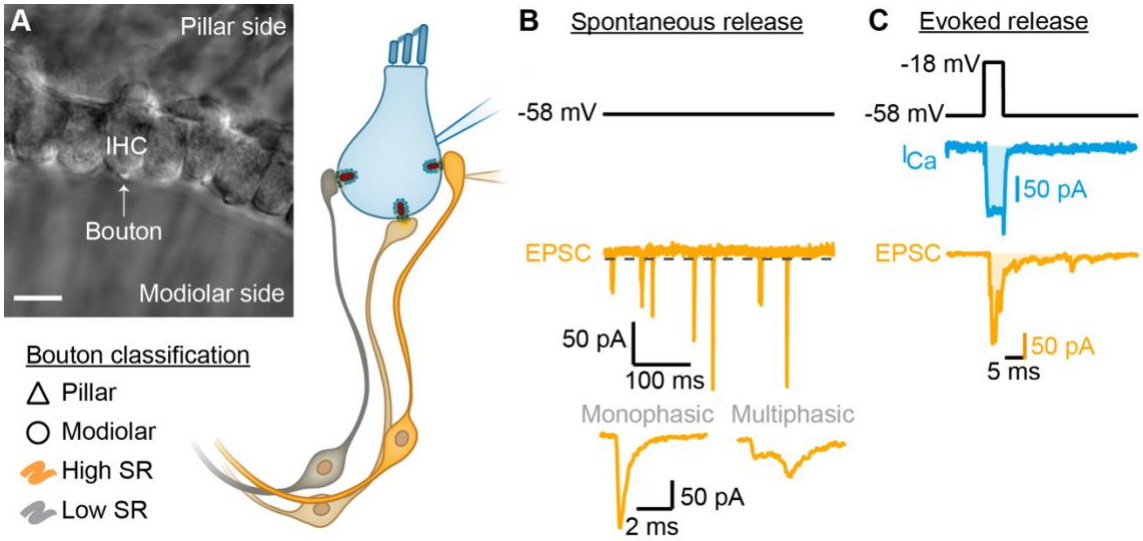

Figure 1. Paired IHC-bouton patch-clamp recordings to study the release properties of individual IHC ribbon synapses as a function of synapse position

A. Differential Interference Contrast (DIC) image of an explanted murine organ of Corti. In this example, supporting cells from the modiolar side were removed to gain access to the IHCs and their contacting boutons. The recorded boutons were classified based on their position (△ pillar or ❍ modiolar) and on their spontaneous rate (*SR*) (**Low *SR*** < 1 EPSC/s vs **High *SR*** ≥ 1 EPSC/s). Scale bar: 10 µm. **B.** Spontaneous release was recorded in absence of stimulation (i.e., IHC holding potential = -58 mV; Supplementary Table 1). sEPSCs were classified as monophasic (a steady rising and monoexponential decay) or as multiphasic (multiple inflections and slowed raising and decaying kinetics). **C.** Evoked release was recorded using depolarizing pulses (black trace), triggering whole IHC Ca^{2+} influx (I_{Ca}, blue trace) and concomitant release of neurotransmitter (eEPSC, light orange trace). Ca^{2+} charge and eEPSC charge were estimated by taking the integral of the current (shaded light blue and light orange areas).

Spontaneous synaptic transmission

To establish the paired recording, we approached boutons facing either the pillar or the modiolar side of the IHC in an effort to elucidate synaptic differences between both sides (Fig. 1A). Due to the technical difficulty of establishing the paired recording, typically only one bouton was recorded per IHC. In order to recapitulate synaptic transmission in the absence of sound stimulation, we held the IHC at their presumed physiological resting potential (-58 mV). To our knowledge, patch-clamp measurements of the IHC resting potential *in vivo* have not yet been accomplished. Classical

intracellular IHC recordings in guinea pig likely resulted in artificially depolarized estimates of the resting potential (-40 to -20 mV, Ref. (Russell & Sellick, 1978)) due to leak conductance introduced by the recording sharp electrodes. Thus, we adhered to the logic of Ref. (Johnson, 2015) and used -58 mV as an operational definition of resting IHC potential. Since $Ca_V1.3$ Ca^{2+}-channels activate at low voltages (-65 to -45 mV (Koschak et al., 2001; Picher, Gehrt, et al., 2017; Platzer et al., 2000; Xu & Lipscombe, 2001)), their open probability at the IHC resting potential is thought to be sufficient to trigger spontaneous release (Glowatzki & Fuchs, 2002; Özçete & Moser, 2020; Robertson & Paki, 2002). Under our experimental conditions, spontaneous, i.e. in the absence of stimulation, excitatory postsynaptic currents (sEPSCs) were observed in 21 of 29 pairs (Fig. 2). We ensured that the recorded postsynaptic activity was not contaminated by voltage-gated Na^+ currents by holding the bouton at -94 mV and including TTX in the bath solution. Amplitudes of sEPSCs typically varied from around -10 pA to -400 pA across all recorded IHC-SGN pairs ("pairs"). The amplitude histogram for all pairs was slightly skewed towards larger amplitudes (skewness of 1.22) with a coefficient of variation (CV) of 0.71. The charge distribution for all pairs displayed a prominent peak at 40 fC, with a skewness of 1.88 and a CV of 0.78. Next, we analyzed the recordings as a function of i) synapse position and ii) rate of spontaneous synaptic transmission.

i) Position dependence of synaptic transmission

From the 29 obtained paired recordings, 18 were classified as pillar synapses. The amplitude (Fig. 2C) and the charge (Fig. 2D) of the sEPSCs were comparable between modiolar and pillar

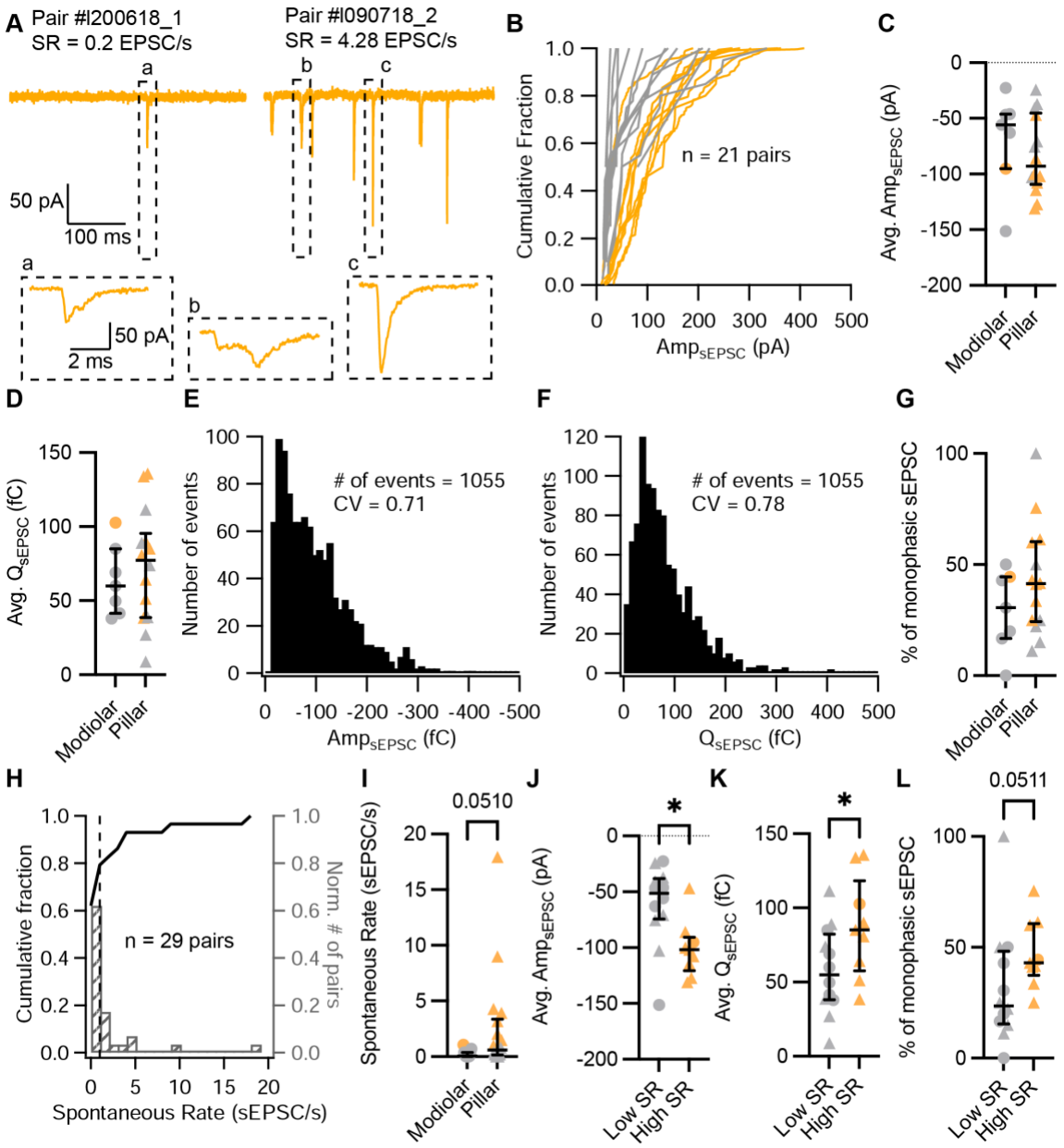

Figure 2. Synapses with high spontaneous release have larger and more compact sEPSCs
A. Spontaneous EPSCs recorded in the absence of stimulation (i.e. IHC holding potential = -58 mV) from two exemplary paired recordings with different spontaneous rate (*SR*). 'Pair #' identifies individual paired recordings. Insets show the selected sEPSCs in an expanded time scale. (a,b) correspond to multiphasic sEPSCs, while (c) represents a typical monophasic sEPSC. **B.** Cumulative sEPSC amplitude plots for 21 paired recordings that had spontaneous release. **C-D.** Average sEPSC amplitude (C) and charge (D) from individual synapses recorded from the pillar or modiolar side of the IHC. **E-F.** Pooled sEPSC amplitude (E) and charge (F) distributions show a distinct peak at -40 pA and 40 pC, respectively. **G.** Percentage of monophasic sEPSCs in pillar and modiolar synapses. **H.** Cumulative fraction (left axis) and normalized histogram (right axis) of the spontaneous rate (bin size is 1 sEPSC/s) of 29 pairs. **I.** Pillar synapses had a strong trend to higher

rates of sEPSCs (p = 0.0510, Mann-Whitney U test). **J-L.** High *SR* synapses had significantly larger sEPSC amplitudes (J; p = 0.0110, unpaired t-test), bigger sEPSC charges (K; p = 0.0464, unpaired t-test) and higher percentages of monophasic sEPSCs (p = 0.0511, Mann-Whitney U test).
Scatter plots represent the 25th, 50th and 75th percentiles with the individual data points overlaid. Synapses were classified as △ pillar or ❍ modiolar, and as Low *SR* < 1 sEPSC/s or High *SR* ≥ 1 sEPSC/s.

SGN boutons (Amp_{sEPSC} -68.74 ± 16.05 pA vs -83.32 ± 9.303 pA, respectively; p = 0.409, unpaired t-test; Q_{sEPSC} 63.67 ± 8.971 fC for modiolar boutons vs 73.44 ± 10.23 fC for pillar boutons; p = 0.5462, unpaired t-test). sEPSC kinetics of pillar SGN boutons showed significantly shorter 10-90% rise times than the modiolar ones (Supplementary Fig. 1A; 0.4001 ± 0.039 ms vs 0.5510 ± 0.059 ms; p = 0.0426, unpaired t-test), yet similar decay times and full-width half-maximum (FWHM) (Supplementary Fig. 1C-E). As a second approach to sEPSC kinetics, we quantified the percentage of monophasic (compact) sEPSCs (Chapochnikov et al., 2014; Glowatzki & Fuchs, 2002). Despite having shorter rise times, pillar SGN boutons had comparable percentages of monophasic sEPSCs (Fig. 2G; p = 0.2018, unpaired t-test).

We then estimated the rate of spontaneous transmission (sEPSC rate, "*SR*") and used it as a surrogate of SGN SR as sEPSCs trigger SGN firing with >90% probability(Rutherford et al., 2012). Given the fact that *ex vivo* experiments can hardly keep the physiological integrity, we expected our estimated rates of sEPSC to underestimate the SGN SR. For each paired recording, we quantified the *SR* during 5 or 10 s of a continuous recording, or during the segment before and after the step depolarization protocols (Supplementary Table 1), in each case at a presynaptic holding potential of -58 mV. *SR* ranged from 0 to about 18 sEPSC/s (Fig. 2H). The *SR* distribution was highly skewed, with a median of 0.2 sEPSC/s and 69% of the pairs with rates lower than 1 sEPSC/s, comparable to the *in vivo* spontaneous firing rate of mouse SGNs (Taberner & Liberman, 2005). *SR* tended to be higher in pairs of the pillar side (mean *SR* of 2.49 ± 1.06 sEPSC/s)

compared to those of the modiolar side (mean *SR* of 0.25 ± 0.107 sEPSC/s; p = 0.0510, Mann-Whitney U test; Fig. 2I).

ii) Relation of synaptic properties to the rate of spontaneous synaptic transmission

Following the spontaneous firing rate classification of SGNs by Taberner and Liberman (2005), we classified the pairs into low (< 1 sEPSC/s) or high (≥ 1 sEPSC/s) *SR* classes. High *SR* pairs had significantly larger sEPSCs (average sEPSC amplitude of -101.2 ± 8.32 pA for high *SR* vs. -61.44 ± 10.46 pA for low *SR*; p = 0.0110, unpaired t-test; Fig. 2J and Supplementary Fig. 1Bi). Likewise, sEPSC charge was significantly larger in high *SR* SGN pairs (Q_{sEPSC} 86.92 ± 11.20 fC for high *SR* vs. 57.64 ± 8.45 fC for low *SR*, p = 0.0464, unpaired t-test; Fig. 2K and Supplementary Fig. 1Bii). The fraction of monophasic sEPSCs tended to be higher in high *SR* pairs, without reaching statistical significance (47.31 ± 5.189% for high SR vs 31.95 ± 7.620% for low SR; p = 0.0511, Mann-Whitney U test; Fig. 2L). sEPSCs kinetics, such as 10-90% rise time, decay time constant and full width-half maximum (Supplementary Fig. 1A), were not different between low and high *SR* pairs (Supplementary Fig. 1F-H). Taken together, these results indicate that high *SR* synapses are characterized by sEPSCs with larger amplitudes and charges, and a relatively more compact waveform. Interestingly, 8 out of 9 high *SR* synapses were located on the pillar side of the IHC.

Evoked synaptic transmission differs between afferent synapses with high and low SR

Next, we compared the physiology of afferent synapses with high and low *SR* by adapting protocols routinely employed for *in vivo* characterization of sound encoding SGNs. For our *ex vivo* paired recordings, we emulate sound stimulation by direct voltage-control of the IHC receptor potential.

i) Stimulus intensity encoding at IHC synapses

Sound intensity encoding by SGNs primarily relies on a spike rate code: their average discharge increases with the strength of the acoustic stimuli from threshold to saturation of the response. These so-called “rate level functions” are typically analyzed by fitting a sigmoidal function, of which the range of sound pressure level between 10 and 90% of the maximal discharge rate represents the operational or dynamic range (Sachs & Abbas, 1974; Taberner & Liberman, 2005; Winter et

al., 1990). To understand stimulus intensity coding at mouse IHC synapses, we measured whole-cell IHC Ca^{2+} currents and the evoked EPSCs (eEPSCs) of single

SGNs in our 29 paired recordings. We stimulated the IHC with 10 ms depolarizations to different potentials ranging from -70 to 0 mV in 5 mV steps (Fig. 3A). We used step depolarizations to emulate physiological receptor potential given that mature IHCs of the “high frequency” mouse cochlea have graded receptor potentials that primarily represent the rectified envelope of an acoustic stimulus (i.e. the DC component (Russell & Sellick, 1978)). At the level of whole-cell Ca^{2+} influx, IHCs with synapses classified as high or low *SR* had similar current-voltage curves. The IHCs had also comparable maximal Ca^{2+} currents (Fig. 3Bi) elicited at similar potentials (Fig. 3Bii) and comparable reversal potentials (Supplementary Fig. 2A). Fractional activation of Ca^{2+} channels was determined from the normalized chord conductance of the IHC. The voltage dependence of Ca^{2+} channel activation was studied by fitting a Boltzmann function to these activation curves (Fig. 3C, upper panel). From these fits, we obtained the voltages of half-maximal activation ($V_{half\ Ca}$) and the sensitivity of the voltage dependence (slope) of the Ca^{2+} channels. “Release-stimulus intensity” curves, akin of an *ex vivo* representation of the SGN rate-level function, were constructed from the normalized Q_{EPSC} (Supplementary Fig. 2B). The voltage dependence of synaptic vesicle release per active zone was approximated by the fit of a sigmoidal function to the individual release-intensity curves (Fig. 3C, lower panel). From these sigmoidal fits, we obtained voltage of 10%-maximal release ($Q_{10,\ EPSC}$), voltage of half-maximal release ($Q_{50,\ EPSC}$), voltage of 90%-maximal release ($Q_{90,\ EPSC}$) and the voltage sensitivity of release (slope). For two low *SR* paired recordings (Fig. 3Dii, grey dotted lines), a sigmoidal function did not properly fit the release-intensity curve (assessed by visual inspection). These pairs were excluded from the statistical analysis.

The whole-cell voltage dependence of Ca^{2+} influx was similar between IHCs contacted by high and low *SR* boutons. The threshold of Ca^{2+} influx (Fig. 3Ei), $V_{half}\ I_{Ca}$ (Fig 3Fi) and voltage sensitivity of

the Ca^{2+} current (Fig. 3Gi) did not differ significantly between IHCs contacted by low or high *SR* synapses.

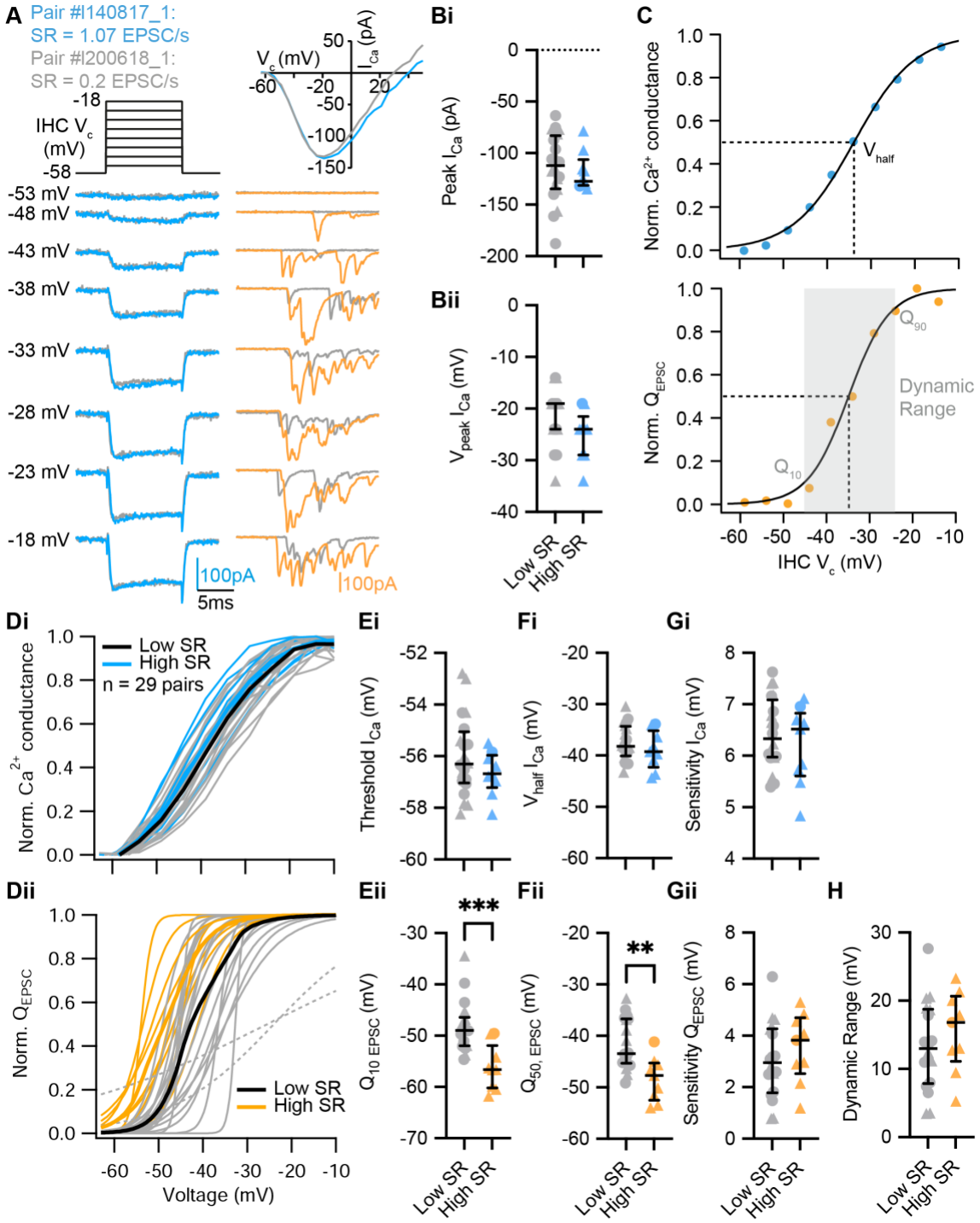

Figure 3. High *SR* synapses have a more hyperpolarized voltage dependence of synaptic release

A. IHC Ca^{2+} current (blue and gray) and eEPSCs (orange and gray) of a high and a low *SR* pair in response to 10 ms depolarizations to different potentials ranging from -58 to -18 mV in 5 mV steps (upper left panel). The upper right panel shows the current-voltage relationships for the two exemplary pairs. **Bi-Bii.** The peak of Ca^{2+} current (Bi) and the voltage eliciting maximum Ca^{2+} current (Bii) were comparable between high and low *SR* synapses. **C.** Upper panel: Fractional activation of the Ca^{2+} channels (blue data points) was obtained from the normalized chord conductance. Voltage of half-maximal activation ($V_{half\ Ca}$) and sensitivity of the voltage dependence (slope *k*) were determined using a Boltzmann fit (black trace) to the activation curve. Lower panel: Release-intensity curves (orange data points) were obtained from the Q_{EPSC} for each depolarization step. A sigmoidal function (black trace) was fitted to obtain the voltage of half-maximal synaptic release (V_{half} Q_{EPSC}) and the voltage sensitivity of the release (slope), as well as the dynamic range for which the exocytosis changes from 10-90% (gray area). **Di-Dii.** Voltage dependence of whole-cell Ca^{2+} channel activation (activation curve; Di) and fits to release-intensity curves (Dii) for 29 pairs of low (< 1 sEPSC/s) and high *SR* (≥ 1 sEPSC/s). Averages (thick lines) and individual curves (thin lines) are overlaid. The release-intensity curve of two pairs could not be fitted (grey dotted lines). **Ei-Gi.** The threshold of Ca^{2+} influx (Ei), V_{half} I_{Ca} (Fi) and voltage sensitivity of I_{Ca} (Gi) did not differ between low and high *SR* synapses. **Eii-Fii**. Voltage of 10% maximum release ($Q_{10\ EPSC}$, Eii; $p = 0.0005$, Mann-Whitney U test) and V_{half} Q_{EPSC} (Fii; $p = 0.0018$, unpaired t-test) were significantly more hyperpolarized in high *SR* synapses. **Gii.** Voltage sensitivity of the release was comparable between low and high *SR* synapses. **H.** Dynamic range release from pairs shown in Dii.
Scatter plots represent the 25th, 50th and 75th percentiles with the individual data points overlaid. Synapses were classified as △ pillar or ❍ modiolar, and as Low *SR* < 1 sEPSC/s or High *SR* ≥ 1 sEPSC/s.

The $Q_{50,\ EPSC}$ of high *SR* synapses (-48.36 ± 1.424 mV) was more hyperpolarized by 6.84 mV compared to low *SR* synapses (-41.52 ± 1.184 mV; $p = 0.0018$, unpaired t-test; Fig. 3Fii). Accordingly, high *SR* synapses had lower thresholds of release than low *SR* synapses (Fig. 3Eii, $Q_{10,\ EPSC}$ of -56.13 ± 1.464 mV vs. -48.20 ± 1.186 mV, $p = 0.0005$, Mann-Whitney U test). The hyperpolarized shift was also significant for $Q_{90\ EPSC}$ (Supplementary Fig.3C). The voltage sensitivity of release, determined by a slope factor, was similar between high and low *SR* synapses (Fig. 3Gii). Dynamic ranges, defined as the voltage range for which the exocytosis changes from 10-90% ($Q_{90\ EPSC} – Q_{10\ EPSC}$), were comparable regardless of the *SR* of the synapses (15.54 ± 1.961 mV for high *SR* synapses vs 13.37 ± 1.519 mV for low *SR* synapses; $p = 0.4065$, unpaired t-test; Fig. 3H). The voltage dependence of Ca^{2+} influx and of synaptic vesicle release did not differ when the synapses where grouped based on their topographical location at the IHC (modiolar vs pillar; Supplementary Fig. 2D-J). All together, these results demonstrate that high *SR* synapses have a

more hyperpolarized voltage-dependence of release, yet comparable dynamic ranges to low *SR* synapses.

ii) Synaptic vesicle pool dynamics at individual IHC active zones

In 13 of the 29 aforementioned paired recordings (6 classified as low *SR* and 7 as high *SR*; 2 belonging to modiolar and 11 to pillar synapses), we employed a forward masking paradigm to study synaptic vesicle (SV) pool dynamics of single afferent synapses. The forward masking paradigm (Harris & Dallos, 1979) is commonly used for *in vivo* analysis of SGN spike rate adaptation and recovery from adaptation, which has been attributed to the depletion of readily releasable pool of SVs (RRP) and the recovery from depletion (Avissar et al., 2013; Frank et al., 2010; Furukawa & Matsuura, 1978; Goutman, 2017; Goutman & Glowatzki, 2007; G.-L. Li et al., 2009; Moser & Beutner, 2000; Schroeder & Hall, 1974). Typically, the *in vivo* protocol is applied at saturating sound pressure levels, which we aimed to mimic using strong step IHC depolarizations (to -18 mV from -58 mV) separated by different interstimulus intervals (ISI: 4, 16, 64 and 256 ms) (Fig. 4A). In analogy to the *in vivo* forward masking paradigm, the first stimulus - called *masker*, as it depresses the response to a subsequent stimulus when applied in rapid succession - had a duration of 100 ms. The second stimulus -denominated *probe*- lasted for 15 ms. The recordings included a time frame of 400 ms preceding the masker and 400 ms following the probe, and the interval between masker and masker was 20 s. Applied to recordings of eEPSCs, the forward masking protocol provides experimental access to the initial RRP release rates, RRP depletion and sustained exocytosis, as well as recovery from RRP depletion. We repeated each protocol several (3 to 20) times, which is important given the stochastic SV release from a finite RRP. Note that we did not employ cyclothiazide to inhibit AMPA receptor desensitization and reduce its contribution to postsynaptic eEPSC depression (Goutman, 2017), given the potential presynaptic effects of cyclothiazide in synaptic release (Diamond & Jahr, 1995; Dittman & Regehr, 1998).

For the analysis of evoked release dynamics, we focused on the response evoked by the masker. We calculated the synaptic delay from the onset of the masker to the onset of the eEPSC. At the presynaptic level, there was no difference in the peak, initial and final IHC Ca^{2+} currents (I_{Ca},

Supplementary Fig. 3A-C) and Ca^{2+} current charge (Q_{Ca}, Fig. 4D) between the recordings from high and low *SR* synapses. High *SR* synapses had significantly shorter synaptic delays (Fig. 4B), with mean latencies of the first eEPSC after stimulus onset of 1.213 ± 0.09 ms compared to 3.341 ± 1.03 ms in low *SR* pairs (p = 0.0221, Mann-Whitney U test). The latency jitter (measured as the standard deviation of the eEPSC latencies; Fig. 4C) was also significantly smaller in high *SR* synapses compared to low *SR* synapses (0.1893 vs 1.769 ms, respectively; p = 0.0012, Mann-Whitney U test). Additionally, high *SR* synapses had significantly larger peak amplitudes of the masker-evoked EPSCs which reports initial RRP release (-421.4 ± 54.22 pA for high SR pairs vs -240.2 ± 23.25 pA for low *SR* pairs; p = 0.0147, unpaired t-test). In contrast, the charge of masker-evoked EPSCs ($Q_{EPSC\ MASKER}$) was more comparable (4.818 ± 0.88 pC for high SR vs 3.223 ± 0.47 pC for low *SR* pairs; p = 0.1574, unpaired t-test; Supplementary Fig. 3D,E). We fitted the first 50 ms of the $Q_{EPSC\ MASKER}$ with the sum of a single exponential and a line function in order to analyze RRP depletion and sustained release (Supplementary Fig. 4G and discontinuous lines in Fig. 4D). The amplitude of the exponential component, thought to reflect RRP exocytosis, was not different between high and low *SR* synapses (Supplementary Fig. 3E; p = 0.4092, unpaired t-test). Likewise, the slope of the linear component, reflecting sustained exocytosis, did not differ significantly between the two groups (Supplementary Fig. 3F; p = 0.1807, Mann-Whitney U test).

To quantify synaptic release in terms of vesicles, we divided $Q_{EPSC\ MASKER}$ by the mean Q_{sEPSC} recorded for each pair. This builds on our assumption that each sEPSC corresponds to a unitary release event ("univesicular mode of release" (Chapochnikov et al., 2014; Grabner & Moser, 2018; Huang & Moser, 2018)). The SV count of the RRP was comparable between high and low *SR* synapses (Fig. 4F, 13.99 ± 2.239 SVs vs 14.28 ± 4.839 SVs, respectively). However, the RRP depleted significantly faster in high *SR* synapses (Fig. 4G): $\tau_{RRP\ depletion}$ was 6.347 ± 1.096 ms for high *SR* vs. 20.88 ± 5.063 ms for low *SR* synapses (p = 0.0140, Mann-Whitney U test). Accordingly, high *SR* synapses showed significantly higher initial release rates compared to low *SR* synapses (2651 ± 660.0 SV/s vs. 927.4 ± 307.4 SV/s; p = 0.0472, unpaired t-test; Fig. 4H). Moreover, high *SR* synapses showed stronger depression of the release rate (Fig. 4J; the ratio of initial/sustained

release rate was 5.941 ± 0.916 for high *SR* pairs and 2.023 ± 0.6251 for low *SR* pairs; $p = 0.006$, unpaired t-test), despite comparable sustained release rates (Fig. 4I; $p = 0.9258$, unpaired t-test).

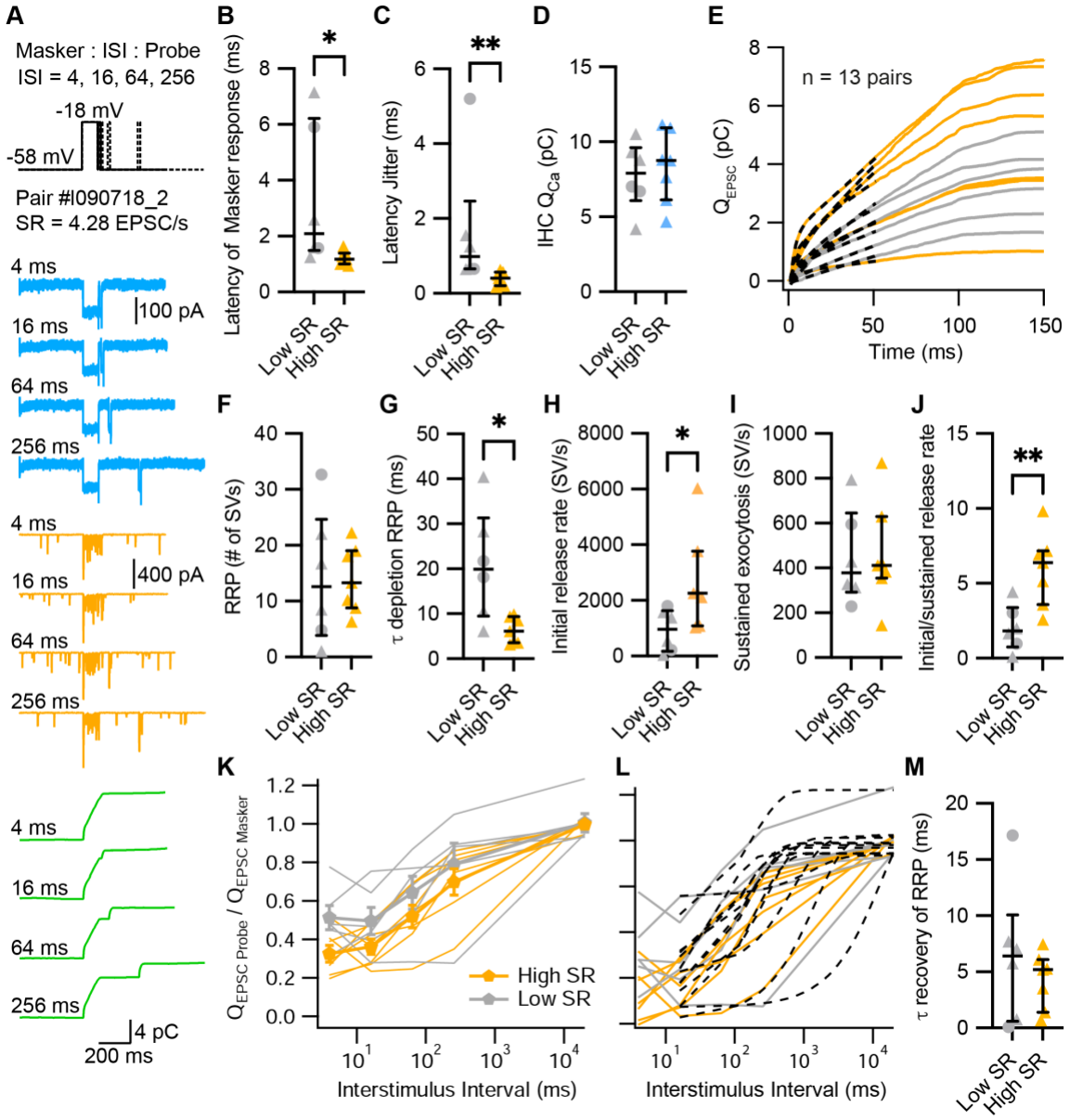

Figure 4. High *SR* synapses have faster evoked release with higher initial release rates
A. Representative responses of Ca^{2+} influx (blue), eEPSC (light orange) and eEPSC charge (Q_{EPSC}, green) to forward masking protocols used to study depression and recovery of RRP. The stimulus (top panel) consists of two sequential voltage steps (masker and probe) separated by different interstimulus intervals (ISI in ms). **B.** Latencies of the evoked EPSCs ($EPSC_{onset}$ - $Masker_{onset}$) were significantly faster in high *SR* than low *SR* synapses ($p = 0.0221$, Mann-Whitney U test). **C.** High *SR* synapses also had less latency jitter ($p = 0.0012$, Mann-Whitney U test). **D.** Presynaptic IHC Ca^{2+} charge (Q_{Ca}) during the masker stimuli was comparable regardless the spontaneous rate of

the recorded postsynaptic bouton. **E.** Pool depletion dynamics were studied by fitting the sum of a single exponential and a line function (black discontinuous line) to the first 50 ms of the average Q_{EPSC} trace in response to the masker stimulus. **F-J.** RRP, time constant (τ) of depletion, initial release rate and sustained release were calculated from the fits and the mean Q_{sEPSC} for each pair. High *SR* synapses depleted the RRP with faster time constants (G; $p = 0.0140$, Mann-Whitney U test) and reached higher initial release rates (H; $p = 0.0472$, unpaired t-test) followed by a stronger adaptation (J; $p = 0.0058$, unpaired t-test). **K.** Recovery from RRP depletion shown as ratio of $Q_{EPSC\ probe}$ and $Q_{EPSC\ masker}$ (mean ± sem) during the first 10 ms of the stimulus. **L.** Single exponential fits from 16 ms to 20000 ms (black dotted lines) to estimate the recovery kinetics from RRP depletion. **M.** Time constant of recovery from RRP depletion obtained from fits in L.
Scatter plots represent the 25th, 50th and 75th percentiles with the individual data points overlaid. Synapses were classified as △ pillar or ❍ modiolar, and as Low *SR* < 1 sEPSC/s or High *SR* ≥ 1 sEPSC/s.

Finally, we determined RRP recovery from depletion using the ratio $Q_{EPSC\ Probe}/Q_{EPSC\ Masker}$, whereby Q_{EPSC} for masker and probe was estimated for the first 10 ms of stimulation. Figure 4K plots the ratio for each interstimulus interval (ISI), including the masker-to-masker interval. Surprisingly, approximately half of the synapses showed a lower ratio at 16 ms than at 4 ms regardless of their *SR*. Therefore, to determine the kinetics of recovery from RRP depletion, we fitted a single exponential to the recovery data over the ISI range from 16 ms to 20 s (Fig. 4L). We did not observe a significant difference between high *SR* and low *SR* synapses (Fig. 4M; $\tau_{recovery\ RRP}$: 4.23 ± 0.94 ms vs 6.413 ± 2.515 ms, respectively; $p = 0.5338$, Mann-Whitney U test). In 4 high *SR* and 4 low *SR* synapses, spontaneous activity was resumed shortly after the offset of the probe. The time to this first sEPSC took longer in high SR synapses compared to low ones (Supplementary Fig. 3F; 185.2 ± 25.25 ms vs 104.5 ± 24.10 ms, respectively; $p = 0.0286$, Mann-Whitney U test).

Discussion

Much of the information on synaptic sound encoding at afferent IHC-SGN synapses has been obtained from either juxtacellular recordings of SGN firing *in vivo* or from *ex vivo* patch-clamp recordings. Yet, it has remained difficult to reconcile those *in vivo* and *ex vivo* results and to establish a unified account of the functional diversity in the auditory nerve. This is due to multiple reasons such as different experimental conditions, animal models and protocols. In this study, we aimed to biophysically characterize the functional heterogeneity of afferent synapses and relate synaptic and SGN firing properties. We performed paired pre- and post-synaptic patch-clamp

recordings from single IHC synapses under near-physiological conditions using protocols adapted from *in vivo* characterization of SGN's response properties. These paired recordings allowed to resolve single release events and to relate spontaneous and evoked transmission in analogy to spontaneous and evoked SGN firing. Using this approach, we were able to distinguish low and high *SR* synapses, likely representing synaptic correlates of low and high SR SGNs. We found that about 89% of high *SR* synapses were located at the pillar side of the IHC. In addition, high *SR* synapses had larger sEPSCs that tended to assume a more compact waveform. High *SR* synapses also had lower voltage-thresholds of release, shorter synaptic delays, and higher initial release rates. RRP size, the rate of sustained exocytosis and the kinetics of RRP recovery from depletion, as well as the dynamic range of release, were comparable between high and low *SR* synapses.

Diversity of spontaneous release and their topographical segregation

The fraction of synapses with a spontaneous release rate higher than 1 sEPSC/s ("high *SR*", 31%, p14-23 mice) compares well to the fraction of high SR SGNs recorded in 8-17-week-old mice *in vivo* (25% of SGNs with SR > 1 spike/s, Taberner & Liberman, 2005). The *SR* range observed in our paired recordings from mouse afferent synapses (0 to 18 EPSC/s) agrees with previous reports of bouton recordings from rat synapses (p15-p17, Wu et al., 2016). However, the maximum rate is considerably smaller than those recorded *in vivo* from single SGNs [up to 60 spikes/s in p14-p21 mice (Wong et al., 2013) and up to 120 spikes/s in 8-17 weeks old mice (Taberner and Liberman, 2005)]. Given that less than 35% of murine SGNs have *in vivo* SRs above 20 spikes/s (Taberner & Liberman, 2005), our lower maximum rate could also originate from a sampling bias. Other important factors that might explain the higher SR reported *in vivo* include: i) the intrinsic biophysical properties of SGNs which could further expand the firing rate distribution (Markowitz & Kalluri, 2020); ii) the developmental recruitment of high SR SGNs with age (Niwa et al., 2021; Romand, 1984; Walsh & McGee, 1987; Wong et al., 2013; Wu et al., 2016); and iii) the partial disruption of the physiological conditions as well as a deviation of the chosen IHC holding potential (aimed to

mimic the IHC resting potential) despite our efforts to mimic physiological conditions during the recordings.

In analogy to the pioneering finding of a synaptic segregation of cat SGNs according to SR along the pillar–modiolar axis of IHCs (M. C. Liberman, 1982; Merchan-Perez & Liberman, 1996), we found that about 89% of high *SR* were located on the pillar IHC side. Yet, not all the synapses of the pillar IHC side had high *SR*. These findings suggests that high frequency and large amplitude of sEPSCs occur predominantly in synapses with smaller ribbons and AZs, opposing results from retinal cells in which smaller ribbons resulted in reduced frequency and amplitude of EPSCs (Mehta et al., 2013). It is important to point out that our modiolar/pillar classification is less precise than that of other studies in which the synapse position was assigned based on a symmetry plane of the IHC (Frank et al., 2009; L. D. Liberman et al., 2011; Ohn et al., 2016; Özçete & Moser, 2020). Moreover, other studies also support an overall pillar-modiolar gradient with “salt and pepper” intermingling of synaptic properties rather than their strict segregation (Ohn et al., 2016; Özçete & Moser, 2020).

Similar to previous reports (Glowatzki & Fuchs, 2002; Grant et al., 2010), we found a high variability in the waveform and amplitude of sEPSCs between synapses, with percentages of monophasic sEPSCs varying between 11 and 100%. Waveform and amplitude of sEPSCs apparently do not depend on the topographical location of the synapse (the present work and Ref. (Niwa et al., 2021)). Yet, high *SR* synapses had a tendency to higher percentages of monophasic sEPSC. The difference in the percentage of monophasic sEPSCs in low and high *SR* synapses could arise from variability in the fusion pore dynamics on the way to vesicle fusion and/or on the number of SVs released in timely manner. In the view of the multivesicular hypothesis of spontaneous release (Glowatzki & Fuchs, 2002; G.-L. Li et al., 2009; Niwa et al., 2021; Schnee et al., 2013), SVs of a modiolar AZ might fuse in an uncoordinated manner, creating a EPSCs with a less compact waveform. Alternatively and our favorite hypothesis, each sEPSC corresponds to a unitary release event (“univesicular mode of release” (Chapochnikov et al., 2014; Grabner & Moser, 2018; Huang & Moser, 2018; Young et al., 2021)) that has the capacity to drive action potential firing (Rutherford

et al., 2012). In the framework of the univesicular hypothesis of spontaneous release, the flickering of the fusion pore, instead of a fusion pore opening followed directly to full vesicle collapse, might be favored in low *SR* synapses, leading to a lower percentage of monophasic sEPSCs. Such heterogeneity of fusion pore dynamics has been reported in chromaffin cells, calyx of Held and hippocampal neurons (Chang et al., 2021; Henkel et al., 2019; Shin et al., 2018, 2020). However, the relation between fusion pore dynamics and spontaneous release rate has not yet been suggested.

Distinct evoked release at low and high SR synapses: potential factors

The temporal and quantal resolution offered by paired recordings allowed us to analyze the biophysical properties of evoked synaptic transmission in relation to the *SR* of the given synapse. In an intriguing resemblance with *in vivo* evoked firing properties of high SR SGNs (Bourien et al., 2014; Buran et al., 2010; Relkin & Doucet, 1991; Rhode & Smith, 1985; Taberner & Liberman, 2005), high *SR* synapses showed lower voltage (~sound pressure *in vivo*) thresholds of synaptic transmission (~firing *in vivo*), shorter and more reliable synaptic latencies (~first spike latencies *in vivo*), and higher initial release rates (~onset firing rate *in vivo*). In addition, we found stronger synaptic depression of high *SR* synapses, which agrees well with the finding of a greater ratio of peak to adapted firing rate in high SR SGNs recorded *in vivo* (Taberner & Liberman, 2005). These results support the hypothesis that IHC synaptic heterogeneity (Frank et al., 2009; Hua et al., 2021; Ohn et al., 2016; Özçete & Moser, 2020; Reijntjes et al., 2020) can account for much of the diversity of spontaneous and sound-evoked SGN firing.

How do high *SR* synapses with likely smaller ribbons and lower maximal Ca^{2+} influx achieve a shorter latency and higher initial release rate? RRP size and SV release probability co-determine neurotransmitter release. Our estimated RRP of about 14 SVs in both high and low *SR* synapses compares well to prior estimates obtained using *ex vivo* electrophysiology (10-40 SVs: Refs. (Goutman & Glowatzki, 2007; Jean et al., 2018; Johnson et al., 2005; Khimich et al., 2005; Moser & Beutner, 2000; Pangrsic et al., 2010; Schnee et al., 2005), model-based analysis of SGN firing (4-40 SVs (Frank et al., 2010; Jean et al., 2018; Peterson et al., 2014)) and electron microscopy

(10-16 SVs within 50 nm of the presynaptic membrane (Chakrabarti et al., 2018; Frank et al., 2010; Graydon et al., 2011; Kantardzhieva et al., 2013; Khimich et al., 2005; Pangrsic et al., 2010). Our comparable RRP size among high and low *SR* synapses indicates that differences in release probability could rather explain different initial release rates.

Release probability of SVs is governed by the number of open Ca^{2+} channels at the AZ (Gratz et al., 2019; Holderith et al., 2012; Scimemi & Diamond, 2012; Sheng et al., 2012; Wong et al., 2013), their spatial coupling to the SV release site (Eggermann et al., 2012; Fekete et al., 2019; Moser et al., 2019; Rebola et al., 2019) and the fusion competence of the SV (Klenchin & Martin, 2000), including the priming and docking state (Lin et al., 2022; Neher & Brose, 2018). Besides the voltage-dependence of Ca^{2+} channel activation, the number of Ca^{2+} channels varies greatly (from approximately 30 to 300) among AZs within one IHC (Neef et al., 2018), with a modiolar-pillar gradient (Frank et al., 2009; Ohn et al., 2016). Interestingly, genetic disruptions that shift the voltage-dependence have a greater impact on the *in vivo* distribution of SR than mutations that change the maximal synaptic Ca^{2+} influx (Jean et al., 2018; Ohn et al., 2016). In addition, a tighter Ca^{2+} control of exocytosis (Ca^{2+} nanodomain) found in pillar synapses (Özçete & Moser, 2020) likely contributes to a greater release probability at high *SR* synapses as observed in the Calyx of Held (Fekete et al., 2019).

In pillar synapses, more hyperpolarized Ca^{2+} channel activation in combination with tighter coupling between the Ca^{2+} channels and the Ca^{2+} sensor of fusion would enable a greater initial release probability for a given stimulus. Moreover, the ensuing Ca^{2+} influx facilitates Ca^{2+} channels and SV priming (Cho & von Gersdorff, 2012; Goutman & Glowatzki, 2007, 2011; Michalski et al., 2017; Moser & Beutner, 2000; Pangrsic et al., 2015; Schnee et al., 2011; Spassova et al., 2004). Such facilitation might contribute to the lower voltage thresholds of synaptic transmission, shorter and more reliable synaptic latencies, and the higher initial release rates observed in high *SR* synapses. Unfortunately, the paired whole-cell presynaptic patch-clamp recordings, as used in the present study, do not allow to resolve Ca^{2+} influx at individual AZs. Even more challenging experiments combining paired recordings, Ca^{2+} imaging, manipulations of Ca^{2+} channels or Ca^{2+} uncaging will

be necessary to further correlate single AZ Ca^{2+} influx, topography of Ca^{2+} channels and SVs, with the dynamics of SV release.

In central glutamatergic synapses, molecular heterogeneity of synaptic proteins plays a critical role in the modulation of SV release probability and priming state (Neher & Brose, 2018; Wichmann & Kuner, 2022). For instance, differential isoforms of priming factors and scaffold proteins have been suggested to tune the functional synaptic diversity of central synapses (Fulterer et al., 2018; Rebola et al., 2019; Rosenmund et al., 2002). Cochlear IHCs have an unconventional fusion machinery that appears to work without neuronal SNARES (Nouvian et al., 2011) and priming factors such as Munc13 and CAPS (Vogl et al., 2015). Therefore, future studies will need to determine the molecular nanoanatomy underlying the specific AZ nanophysiology and functional synaptic heterogeneity at IHCs. Promising candidates include RBPs (Butola et al., 2021; Grauel et al., 2016; Krinner et al., 2017, 2021; Petzoldt et al., 2020), RIMs (Jung et al., 2015; Picher, Oprişoreanu, et al., 2017), and Septin (Fekete et al., 2019; Yang et al., 2010).

Challenges for relating synaptic and neural response properties

Next to providing support for the presynaptic hypothesis of functional SGN diversity, the present study also highlights some of the challenges met when aiming to bridge the gap between presynaptic hair cell function and neural sound encoding. Despite major efforts undertaken to match experimental conditions and protocols, it remains difficult to reconcile some findings of *ex vivo* and *in vivo* physiology. Parameters such as RRP size (~# spikes of the rapidly adapting component of firing), sustained exocytosis (~adapted firing rate *in vivo*), recovery of spontaneous and evoked release (~recovery from forward masking *in vivo*) did not differ among our high and low *SR* synapses, and contrasts with *in vivo* data (e.g. Refs. (Bourien et al., 2014; Buran et al., 2010; Relkin & Doucet, 1991; Rhode & Smith, 1985; Taberner & Liberman, 2005)).

Of particular interest is that low and high *SR* synapses in our study show comparable dynamic ranges and voltage sensitivity (slope) of release-intensity. This diverges from *in vivo* high SR SGNs with smaller dynamic ranges and steeper slopes than the low SR ones (Ohlemiller et al., 1991;

Winter et al., 1990). Could this reflect the non-linear saturating properties of the basilar membrane (Sachs et al., 1989; Sachs & Abbas, 1974; Yates et al., 1990) (discussed in Ref. (Ohlemiller et al., 1991)) which might widen the rate level function of low SR SGNs? It remains to be determined whether this and the other aforementioned differences between our data and *in vivo* reports could be attributed to mechanisms downstream of glutamate release and AMPA receptor activation. The possible mechanisms include but are not limited to: i) partial depletion of the "standing" RRP (i.e. the occupancy of the RRP release sites with a fusion-competent SV (Moser, 2020; Pangrsic et al., 2010)) at high *SR* synapses; ii) differences in SGN excitability (Crozier & Davis, 2014; Markowitz & Kalluri, 2020; Smith et al., 2015) due to heterogenous molecular (Petitpré et al., 2018, 2020; Shrestha et al., 2018; Sun et al., 2018) and morphological profiles (M. C. Liberman, 1980; Merchan-Perez & Liberman, 1996; Tsuji & Liberman, 1997); and iii) differences in efferent innervation of SGNs (Hua et al., 2021; M. C. Liberman, 1990; Ruel et al., 2001; Wu et al., 2020; Yin et al., 2014). Certainly, caution is to be applied for the comparison of *ex vivo* and *in vivo* data due to partial disruption of the physiological milieu despite our efforts to maintain near-physiological conditions.

Clearly more work is needed to elucidate the mechanisms of SGN firing diversity in the cochlea. Ideally, future studies will combine *in vivo* and *ex vivo* experiments, such as combining physiological SGN characterization with neural backtracing and synaptic morphology of labelled SGNs using volume imaging of afferent and efferent connectivity (Hua et al., 2021). Moreover, combining optogenetic IHC stimulation with imaging of SGN activity could provide higher throughput and serve posthoc morphology. Finally, paired patch-clamp recordings, as done in the present study, could be combined with fiber tracing and immunolabeling to bridge the gap between synaptic transmission and SGN neurophysiology.

Materials and Methods

We aimed to mimic physiological conditions as closely as possible during our *ex vivo* experiments.

We aimed to mimic physiological conditions as closely as possible during our *ex vivo* experiments. Simultaneous paired patch-clamp recordings from IHCs and one of the postsynaptic SGN boutons were performed on mice after the onset of hearing (postnatal days (p) 14-23). We performed perforated-patch whole-cell configuration from IHCs, held at their physiological resting potential (-58 mV), and ruptured-patch whole-cell recordings from one of the postsynaptic SGN boutons (Fig. 1). Recordings were made at body temperature and in artificial perilymph-like solution (Wangemann & Schacht, 1996). The recorded boutons were classified based on their position (△ pillar or ❍ modiolar) and on their spontaneous rate (*SR*) (**Low *SR*** < 1 EPSC/s vs **High *SR*** $\geq$ 1 EPSC/s). For a detailed description of the methods, see SI Materials and Methods.

Acknowledgments

We would like to thank Dr. Chao-Hua Huang and Dr. Jakob Neef for their experimental and analytical input. Dr. Antoine Huet for the discussion regarding *in vivo* response properties of spiral ganglion neurons. Dres. Erwin Neher and Manfred Lindau for critical input into this project. LMJT is a recipient of the Erwin Neher Fellowship and T.M. is a Max-Planck Fellow at the Max Planck Institute for Multidisciplinary Sciences. This work was further supported by the Deutsche Forschungsgemeinschaft (DFG, German Research Foundation) via the Collaborative Research Center 889 (project A02) and the Leibniz Program (MO896/5 to T.M). This research was further supported by Fondation Pour l'Audition (FPA RD-2020-10). LMJT is a member of the Hertha Sponer College from the Cluster of Excellence Multiscale Bioimaging (MBExC).

References

Avissar, M., Wittig, J. H., Saunders, J. C., & Parsons, T. D. (2013). Refractoriness Enhances Temporal Coding by Auditory Nerve Fibers. *Journal of Neuroscience*, *33*(18), 7681–7690. https://doi.org/10.1523/JNEUROSCI.3405-12.2013

Barbary, A. E. (1991). Auditory nerve of the normal and jaundiced rat. I. Spontaneous discharge rate and cochlear nerve histology. *Hearing Research*, *54*(1), 75–90. https://doi.org/10.1016/0378-5955(91)90138-Y

Bourien, J., Tang, Y., Batrel, C., Huet, A., Lenoir, M., Ladrech, S., Desmadryl, G., Nouvian, R., Puel, J.-L., & Wang, J. (2014). Contribution of auditory nerve fibers to compound action potential of the auditory nerve. *Journal of Neurophysiology*, *112*(5), 1025–1039. https://doi.org/10.1152/jn.00738.2013

Buran, B. N., Strenzke, N., Neef, A., Gundelfinger, E. D., Moser, T., & Liberman, M. C. (2010). Onset coding is degraded in auditory nerve fibers from mutant mice lacking synaptic ribbons. *The Journal of Neuroscience: The Official Journal of the Society for Neuroscience*, *30*(22), 7587–7597. https://doi.org/10.1523/JNEUROSCI.0389-10.2010

Butola, T., Alvanos, T., Hintze, A., Koppensteiner, P., Kleindienst, D., Shigemoto, R., Wichmann, C., & Moser, T. (2021). RIM-Binding Protein 2 Organizes Ca2+ Channel Topography and Regulates Release Probability and Vesicle Replenishment at a Fast Central Synapse. *Journal of Neuroscience*, *41*(37), 7742–7767. https://doi.org/10.1523/JNEUROSCI.0586-21.2021

Chakrabarti, R., Michanski, S., & Wichmann, C. (2018). Vesicle sub-pool organization at inner hair cell ribbon synapses. *EMBO Reports*, e44937. https://doi.org/10.15252/embr.201744937

Chang, C.-W., Hsiao, Y.-T., & Jackson, M. B. (2021). Synaptophysin Regulates Fusion Pores and Exocytosis Mode in Chromaffin Cells. *Journal of Neuroscience*, *41*(16), 3563–3578. https://doi.org/10.1523/JNEUROSCI.2833-20.2021

Chapochnikov, N. M., Takago, H., Huang, C.-H., Pangršič, T., Khimich, D., Neef, J., Auge, E., Göttfert, F., Hell, S. W., Wichmann, C., Wolf, F., & Moser, T. (2014). Uniquantal Release through a Dynamic Fusion Pore Is a Candidate Mechanism of Hair Cell Exocytosis. *Neuron*, *17*(83), 1389–1403. https://doi.org/10.1016/j.neuron.2014.08.003

Cho, S., & von Gersdorff, H. (2012). Ca2+ influx and neurotransmitter release at ribbon synapses. *Cell Calcium*, *52*(3–4), 208–216. https://doi.org/10.1016/j.ceca.2012.06.004

Crozier, R. A., & Davis, R. L. (2014). Unmasking of Spiral Ganglion Neuron Firing Dynamics by Membrane Potential and Neurotrophin-3. *Journal of Neuroscience*, *34*(29), 9688–9702. https://doi.org/10.1523/JNEUROSCI.4552-13.2014

Diamond, J. S., & Jahr, C. E. (1995). Asynchronous release of synaptic vesicles determines the time course of the AMPA receptor-mediated EPSC. *Neuron*, *15*(5), 1097–1107.

Dittman, J. S., & Regehr, W. G. (1998). Calcium Dependence and Recovery Kinetics of Presynaptic Depression at the Climbing Fiber to Purkinje Cell Synapse. *The Journal of Neuroscience*, *18*(16), 6147–6162.

Eggermann, E., Bucurenciu, I., Goswami, S. P., & Jonas, P. (2012). Nanodomain coupling between Ca^{2+} channels and sensors of exocytosis at fast mammalian synapses. *Nature Reviews Neuroscience*, *13*(1), 7–21. https://doi.org/10.1038/nrn3125

Evans, E. F. (1972). The frequency response and other properties of single fibres in the guinea-pig cochlear nerve. *The Journal of Physiology*, *226*(1), 263–287. https://doi.org/10.1113/jphysiol.1972.sp009984

Fekete, A., Nakamura, Y., Yang, Y.-M., Herlitze, S., Mark, M. D., DiGregorio, D. A., & Wang, L.-Y. (2019). Underpinning heterogeneity in synaptic transmission by presynaptic ensembles of distinct morphological modules. *Nature Communications*, *10*(1), 826. https://doi.org/10.1038/s41467-019-08452-2

Frank, T., Khimich, D., Neef, A., & Moser, T. (2009). Mechanisms contributing to synaptic Ca2+ signals and their heterogeneity in hair cells. *Proceedings of the National Academy of Sciences*, *106*(11), 4483–4488. https://doi.org/10.1073/pnas.0813213106

Frank, T., Rutherford, M. A., Strenzke, N., Neef, A., Pangršič, T., Khimich, D., Fejtova, A., Gundelfinger, E. D., Liberman, M. C., Harke, B., Bryan, K. E., Lee, A., Egner, A., Riedel, D., & Moser, T. (2010). Bassoon and the synaptic ribbon organize Ca^{2+} channels and vesicles to add release sites and promote refilling. *Neuron*, *68*(4), 724–738. https://doi.org/10.1016/j.neuron.2010.10.027

Fulterer, A., Andlauer, T. F. M., Ender, A., Maglione, M., Eyring, K., Woitkuhn, J., Lehmann, M., Matkovic-Rachid, T., Geiger, J. R. P., Walter, A. M., Nagel, K. I., & Sigrist, S. J. (2018). Active Zone Scaffold Protein Ratios Tune Functional Diversity across Brain Synapses. *Cell Reports*, *23*(5), 1259–1274. https://doi.org/10.1016/j.celrep.2018.03.126

Furukawa, T., & Matsuura, S. (1978). Adaptive rundown of excitatory post-synaptic potentials at synapses between hair cells and eight nerve fibres in the goldfish. *The Journal of Physiology*, *276*, 193–209.

Glowatzki, E., & Fuchs, P. A. (2002). Transmitter release at the hair cell ribbon synapse. *Nature Neuroscience*, *5*(2), 147–154. https://doi.org/10.1038/nn796

Gómez-Casati, M. E., & Goutman, J. D. (2021). Divide and conquer acoustic diversity. *The EMBO Journal*, *40*(5), e107531. https://doi.org/10.15252/embj.2020107531

Goutman, J. D. (2017). Mechanisms of synaptic depression at the hair cell ribbon synapse that support auditory nerve function. *Proceedings of the National Academy of Sciences of the United States of America*. https://doi.org/10.1073/pnas.1706160114

Goutman, J. D., & Glowatzki, E. (2007). Time course and calcium dependence of transmitter release at a single ribbon synapse. *Proceedings of the National Academy of Sciences*, *104*(41), 16341–16346. https://doi.org/10.1073/pnas.0705756104

Goutman, J. D., & Glowatzki, E. (2011). Short-Term Facilitation Modulates Size and Timing of the Synaptic Response at the Inner Hair Cell Ribbon Synapse. *The Journal of Neuroscience*, *31*(22), 7974–7981. https://doi.org/10.1523/JNEUROSCI.0604-11.2011

Grabner, C. P., & Moser, T. (2018). Individual synaptic vesicles mediate stimulated exocytosis from cochlear inner hair cells. *Proceedings of the National Academy of Sciences*, *115*(50), 12811–12816. https://doi.org/10.1073/pnas.1811814115

Grant, L., Yi, E., & Glowatzki, E. (2010). Two Modes of Release Shape the Postsynaptic Response at the Inner Hair Cell Ribbon Synapse. *The Journal of Neuroscience*, *30*(12), 4210–4220. https://doi.org/10.1523/JNEUROSCI.4439-09.2010

Gratz, S. J., Goel, P., Bruckner, J. J., Hernandez, R. X., Khateeb, K., Macleod, G. T., Dickman, D., & O'Connor-Giles, K. M. (2019). Endogenous Tagging Reveals Differential Regulation of Ca2+ Channels at Single Active Zones during Presynaptic Homeostatic Potentiation and Depression. *Journal of Neuroscience*, *39*(13), 2416–2429. https://doi.org/10.1523/JNEUROSCI.3068-18.2019

Grauel, M. K., Maglione, M., Reddy-Alla, S., Willmes, C. G., Brockmann, M. M., Trimbuch, T., Rosenmund, T., Pangalos, M., Vardar, G., Stumpf, A., Walter, A. M., Rost, B. R., Eickholt, B. J., Haucke, V., Schmitz, D., Sigrist, S. J., & Rosenmund, C. (2016). RIM-binding protein

2 regulates release probability by fine-tuning calcium channel localization at murine hippocampal synapses. *Proceedings of the National Academy of Sciences*, *113*(41), 11615–11620. https://doi.org/10.1073/pnas.1605256113

Graydon, C. W., Cho, S., Li, G.-L., Kachar, B., & von Gersdorff, H. (2011). Sharp Ca2+ Nanodomains beneath the Ribbon Promote Highly Synchronous Multivesicular Release at Hair Cell Synapses. *The Journal of Neuroscience*, *31*(46), 16637–16650. https://doi.org/10.1523/JNEUROSCI.1866-11.2011

Harris, D. M., & Dallos, P. (1979). Forward masking of auditory nerve fiber responses. *Journal of Neurophysiology*, *42*(4), 1083–1107.

Henkel, A. W., Mouihate, A., & Welzel, O. (2019). Differential Release of Exocytosis Marker Dyes Indicates Stimulation-Dependent Regulation of Synaptic Activity. *Frontiers in Neuroscience*, *13*. https://www.frontiersin.org/article/10.3389/fnins.2019.01047

Holderith, N., Lorincz, A., Katona, G., Rózsa, B., Kulik, A., Watanabe, M., & Nusser, Z. (2012). Release probability of hippocampal glutamatergic terminals scales with the size of the active zone. *Nature Neuroscience*, *15*(7), 988–997. https://doi.org/10.1038/nn.3137

Hua, Y., Ding, X., Wang, H., Wang, F., Lu, Y., Neef, J., Gao, Y., Moser, T., & Wu, H. (2021). Electron Microscopic Reconstruction of Neural Circuitry in the Cochlea. *Cell Reports*, *34*(1). https://doi.org/10.1016/j.celrep.2020.108551

Huang, C.-H., & Moser, T. (2018). Ca2+ Regulates the Kinetics of Synaptic Vesicle Fusion at the Afferent Inner Hair Cell Synapse. *Frontiers in Cellular Neuroscience*, *12*, 364. https://doi.org/10.3389/fncel.2018.00364

Huet, A., Batrel, C., Tang, Y., Desmadryl, G., Wang, J., Puel, J.-L., & Bourien, J. (2016). Sound coding in the auditory nerve of gerbils. *Hearing Research*. https://doi.org/10.1016/j.heares.2016.05.006

Jean, P., Morena, D. L. de la, Michanski, S., Tobón, L. M. J., Chakrabarti, R., Picher, M. M., Neef, J., Jung, S., Gültas, M., Maxeiner, S., Neef, A., Wichmann, C., Strenzke, N., Grabner, C., & Moser, T. (2018). The synaptic ribbon is critical for sound encoding at high rates and with temporal precision. *ELife*, *7*, e29275. https://doi.org/10.7554/eLife.29275

Johnson, S. L. (2015). Membrane properties specialize mammalian inner hair cells for frequency or intensity encoding. *ELife*, *4*, e08177. https://doi.org/10.7554/eLife.08177

Johnson, S. L., Marcotti, W., & Kros, C. J. (2005). Increase in efficiency and reduction in Ca2+ dependence of exocytosis during development of mouse inner hair cells. *The Journal of Physiology*, *563*(1), 177–191. https://doi.org/10.1113/jphysiol.2004.074740

Jung, S., Oshima-Takago, T., Chakrabarti, R., Wong, A. B., Jing, Z., Yamanbaeva, G., Picher, M. M., Wojcik, S. M., Göttfert, F., Predoehl, F., Michel, K., Hell, S. W., Schoch, S., Strenzke, N., Wichmann, C., & Moser, T. (2015). Rab3-interacting molecules 2α and 2β promote the abundance of voltage-gated CaV1.3 Ca2+ channels at hair cell active zones. *Proceedings of the National Academy of Sciences*, *112*(24), E3141–E3149. https://doi.org/10.1073/pnas.1417207112

Kantardzhieva, A. V., Liberman, M. C., & Sewell, W. F. (2013). Quantitative analysis of ribbons, vesicles, and cisterns at the cat inner hair cell synapse: Correlations with spontaneous rate. *The Journal of Comparative Neurology*, *521*(14), 3260–3271. https://doi.org/10.1002/cne.23345

Khimich, D., Nouvian, R., Pujol, R., tom Dieck, S., Egner, A., Gundelfinger, E. D., & Moser, T. (2005). Hair cell synaptic ribbons are essential for synchronous auditory signalling. *Nature*, *434*(7035), 889–894. https://doi.org/10.1038/nature03418

Kiang, N. Y. S., Watanabe, T., Thomas, E.C., & Clark, L.F. (1965). *Discharge Patterns of Single Fibers in the Cat's Auditory Nerve*. MIT Press.

Klenchin, V. A., & Martin, T. F. J. (2000). Priming in exocytosis: Attaining fusion-competence after vesicle docking. *Biochimie*, *82*(5), 399–407. https://doi.org/10.1016/S0300-9084(00)00208-X

Koschak, A., Reimer, D., Huber, I., Grabner, M., Glossmann, H., Engel, J., & Striessnig, J. (2001). Alpha 1D (Cav1.3) subunits can form l-type Ca2+ channels activating at negative voltages. *The Journal of Biological Chemistry*, *276*(25), 22100–22106. https://doi.org/10.1074/jbc.M101469200

Krinner, S., Butola, T., Jung, S., Wichmann, C., & Moser, T. (2017). RIM-Binding Protein 2 Promotes a Large Number of CaV1.3 Ca2+-Channels and Contributes to Fast Synaptic Vesicle Replenishment at Hair Cell Active Zones. *Frontiers in Cellular Neuroscience*, *11*, 334. https://doi.org/10.3389/fncel.2017.00334

Krinner, S., Predoehl, F., Burfeind, D., Vogl, C., & Moser, T. (2021). RIM-Binding Proteins Are Required for Normal Sound-Encoding at Afferent Inner Hair Cell Synapses. *Frontiers in Molecular Neuroscience*, *14*, 651935. https://doi.org/10.3389/fnmol.2021.651935

Li, C., Li, X., Bi, Z., Sugino, K., Wang, G., Zhu, T., & Liu, Z. (2020). Comprehensive transcriptome analysis of cochlear spiral ganglion neurons at multiple ages. *ELife*, *9*. https://doi.org/10.7554/eLife.50491

Li, G.-L., Keen, E., Andor-Ardo, D., Hudspeth, A. J., & von Gersdorff, H. (2009). The Unitary Event Underlying Multiquantal EPSCs at a Hair Cell's Ribbon Synapse. *Journal of Neuroscience*, *29*(23), 7558–7568. https://doi.org/10.1523/JNEUROSCI.0514-09.2009

Liberman, L. D., Wang, H., & Liberman, M. C. (2011). Opposing Gradients of Ribbon Size and AMPA Receptor Expression Underlie Sensitivity Differences among Cochlear-Nerve/Hair-Cell Synapses. *The Journal of Neuroscience*, *31*(3), 801–808. https://doi.org/10.1523/JNEUROSCI.3389-10.2011

Liberman, M. C. (1980). Morphological differences among radial afferent fibers in the cat cochlea: An electron-microscopic study of serial sections. *Hearing Research*, *3*(1), 45–63. https://doi.org/10.1016/0378-5955(80)90007-6

Liberman, M. C. (1982). Single-Neuron Labeling in the Cat Auditory Nerve. *Science*, *216*(4551), 1239–1241. https://doi.org/10.1126/science.7079757

Liberman, M. C. (1990). Effects of chronic cochlear de-efferentation on auditory-nerve response. *Hearing Research*, *49*(1–3), 209–223.

Lin, K.-H., Taschenberger, H., & Neher, E. (2022). A sequential two-step priming scheme reproduces diversity in synaptic strength and short-term plasticity. *Proceedings of the National Academy of Sciences*, *119*(34), e2207987119. https://doi.org/10.1073/pnas.2207987119

Markowitz, A. L., & Kalluri, R. (2020). Gradients in the biophysical properties of neonatal auditory neurons align with synaptic contact position and the intensity coding map of inner hair cells. *ELife*, *9*, e55378. https://doi.org/10.7554/eLife.55378

Mehta, B., Snellman, J., Chen, S., Li, W., & Zenisek, D. (2013). Synaptic Ribbons Influence the Size and Frequency of Miniature-like Evoked Postsynaptic Currents. *Neuron*, *77*(3), 516–527. https://doi.org/10.1016/j.neuron.2012.11.024

Merchan-Perez, A., & Liberman, M. C. (1996). Ultrastructural differences among afferent synapses on cochlear hair cells: Correlations with spontaneous discharge rate. *The Journal of Comparative Neurology*, *371*(2), 208–221. https://doi.org/10.1002/(SICI)1096-9861(19960722)371:2<208::AID-CNE2>3.0.CO;2-6

Meyer, A. C., Frank, T., Khimich, D., Hoch, G., Riedel, D., Chapochnikov, N. M., Yarin, Y. M., Harke, B., Hell, S. W., Egner, A., & Moser, T. (2009). Tuning of synapse number, structure and function in the cochlea. *Nature Neuroscience*, *12*(4), 444–453. https://doi.org/10.1038/nn.2293

Meyer, A. C., & Moser, T. (2010). Structure and function of cochlear afferent innervation. *Current Opinion in Otolaryngology & Head and Neck Surgery*, *18*(5), 441–446. https://doi.org/10.1097/MOO.0b013e32833e0586

Michalski, N. A., Goutman, J. D., Auclair, S. M., Monvel, J. B. de, Tertrais, M., Emptoz, A., Parrin, A., Nouaille, S., Guillon, M., Sachse, M., Ciric, D., Bahloul, A., Hardelin, J.-P., Sutton, R. B., Avan, P., Krishnakumar, S. S., Rothman, J. E., Dulon, D., Safieddine, S., & Petit, C. (2017). Otoferlin acts as a Ca2+ sensor for vesicle fusion and vesicle pool replenishment at auditory hair cell ribbon synapses. *ELife*, *6*, e31013. https://doi.org/10.7554/eLife.31013

Moser, T. (2020). Presynaptic Physiology of Cochlear Inner Hair Cells. In *The Senses: A Comprehensive Reference* (pp. 441–467). Elsevier. https://doi.org/10.1016/B978-0-12-809324-5.24185-0

Moser, T., & Beutner, D. (2000). Kinetics of exocytosis and endocytosis at the cochlear inner hair cell afferent synapse of the mouse. *Proceedings of the National Academy of Sciences*, *97*(2), 883–888. https://doi.org/10.1073/pnas.97.2.883

Moser, T., Grabner, C. P., & Schmitz, F. (2019). Sensory processing at ribbon synapses in the retina and the cochlea. *Physiological Reviews*, *100*(1), 103–144. https://doi.org/10.1152/physrev.00026.2018

Moser, T., Neef, A., & Khimich, D. (2006). Mechanisms underlying the temporal precision of sound coding at the inner hair cell ribbon synapse. *The Journal of Physiology*, *576*(1), 55–62. https://doi.org/10.1113/jphysiol.2006.114835

Neef, J., Urban, N. T., Ohn, T.-L., Frank, T., Jean, P., Hell, S. W., Willig, K. I., & Moser, T. (2018). Quantitative optical nanophysiology of Ca^{2+} signaling at inner hair cell active zones. *Nature Communications*, *9*(1), 290. https://doi.org/10.1038/s41467-017-02612-y

Neher, E., & Brose, N. (2018). Dynamically Primed Synaptic Vesicle States: Key to Understand Synaptic Short-Term Plasticity. *Neuron*, *100*(6), 1283–1291. https://doi.org/10.1016/j.neuron.2018.11.024

Niwa, M., Young, E. D., Glowatzki, E., & Ricci, A. J. (2021). Functional subgroups of cochlear inner hair cell ribbon synapses differently modulate their EPSC properties in response to stimulation. *Journal of Neurophysiology*, *125*(6), 2461–2479. https://doi.org/10.1152/jn.00452.2020

Nouvian, R., Neef, J., Bulankina, A. V., Reisinger, E., Pangršič, T., Frank, T., Sikorra, S., Brose, N., Binz, T., & Moser, T. (2011). Exocytosis at the hair cell ribbon synapse apparently operates without neuronal SNARE proteins. *Nature Neuroscience*, *14*(4), 411–413. https://doi.org/10.1038/nn.2774

Nusser, Z. (2018). Creating diverse synapses from the same molecules. *Current Opinion in Neurobiology*, *51*, 8–15. https://doi.org/10.1016/j.conb.2018.01.001

Ohlemiller, K. K., Echteler, S. M., & Siegel, J. H. (1991). Factors that influence rate-versus-intensity relations in single cochlear nerve fibers of the gerbil. *The Journal of the Acoustical Society of America*, *90*(1), 274–287. https://doi.org/10.1121/1.401298

Ohn, T.-L., Rutherford, M. A., Jing, Z., Jung, S., Duque-Afonso, C. J., Hoch, G., Picher, M. M., Scharinger, A., Strenzke, N., & Moser, T. (2016). Hair cells use active zones with different voltage dependence of Ca^{2+} influx to decompose sounds into complementary neural codes. *Proceedings of the National Academy of Sciences*, *113*(32), E4716–E4725. https://doi.org/10.1073/pnas.1605737113

Özçete, Ö. D., & Moser, T. (2020). A sensory cell diversifies its output by varying Ca^{2+} influx-release coupling among active zones. *The EMBO Journal*. https://doi.org/10.15252/embj.2020106010

Pangrsic, T., Gabrielaitis, M., Michanski, S., Schwaller, B., Wolf, F., Strenzke, N., & Moser, T. (2015). EF-hand protein Ca2+ buffers regulate Ca2+ influx and exocytosis in sensory hair cells. *Proceedings of the National Academy of Sciences of the United States of America*, *112*(9), E1028–E1037. https://doi.org/10.1073/pnas.1416424112

Pangrsic, T., Lasarow, L., Reuter, K., Takago, H., Schwander, M., Riedel, D., Frank, T., Tarantino, L. M., Bailey, J. S., Strenzke, N., Brose, N., Müller, U., Reisinger, E., & Moser, T. (2010). Hearing requires otoferlin-dependent efficient replenishment of synaptic vesicles in hair cells. *Nature Neuroscience*, *13*(7), 869–876. https://doi.org/jung 2015

Peterson, A. J., Irvine, D. R. F., & Heil, P. (2014). A model of synaptic vesicle-pool depletion and replenishment can account for the interspike interval distributions and nonrenewal

properties of spontaneous spike trains of auditory-nerve fibers. *The Journal of Neuroscience: The Official Journal of the Society for Neuroscience*, *34*(45), 15097–15109. https://doi.org/10.1523/JNEUROSCI.0903-14.2014

Petitpré, C., Bourien, J., Wu, H., Diuba, A., Puel, J.-L., & Lallemend, F. (2020). Genetic and functional diversity of primary auditory afferents. *Current Opinion in Physiology*, *18*, 85–94. https://doi.org/10.1016/j.cophys.2020.09.011

Petitpré, C., Wu, H., Sharma, A., Tokarska, A., Fontanet, P., Wang, Y., Helmbacher, F., Yackle, K., Silberberg, G., Hadjab, S., & Lallemend, F. (2018). Neuronal heterogeneity and stereotyped connectivity in the auditory afferent system. *Nature Communications*, *9*(1), 3691. https://doi.org/10.1038/s41467-018-06033-3

Petzoldt, A. G., Götz, T. W. B., Driller, J. H., Lützkendorf, J., Reddy-Alla, S., Matkovic-Rachid, T., Liu, S., Knoche, E., Mertel, S., Ugorets, V., Lehmann, M., Ramesh, N., Beuschel, C. B., Kuropka, B., Freund, C., Stelzl, U., Loll, B., Liu, F., Wahl, M. C., & Sigrist, S. J. (2020). RIM-binding protein couples synaptic vesicle recruitment to release sites. *Journal of Cell Biology*, *219*(7), e201902059. https://doi.org/10.1083/jcb.201902059

Picher, M. M., Gehrt, A., Meese, S., Ivanovic, A., Predoehl, F., Jung, S., Schrauwen, I., Dragonetti, A. G., Colombo, R., Camp, G. V., Strenzke, N., & Moser, T. (2017). Ca2+-binding protein 2 inhibits Ca2+-channel inactivation in mouse inner hair cells. *Proceedings of the National Academy of Sciences*, *114*(9), E1717–E1726. https://doi.org/10.1073/pnas.1617533114

Picher, M. M., Oprişoreanu, A.-M., Jung, S., Michel, K., Schoch, S., & Moser, T. (2017). Rab Interacting Molecules 2 and 3 Directly Interact with the Pore-Forming CaV1.3 Ca2+ Channel Subunit and Promote Its Membrane Expression. *Frontiers in Cellular Neuroscience*, *11*. https://doi.org/10.3389/fncel.2017.00160

Platzer, J., Engel, J., Schrott-Fischer, A., Stephan, K., Bova, S., Chen, H., Zheng, H., & Striessnig, J. (2000). Congenital deafness and sinoatrial node dysfunction in mice lacking class D L-type Ca^{2+} channels. *Cell*, *102*(1), 89–97.

Rebola, N., Reva, M., Kirizs, T., Szoboszlay, M., Lőrincz, A., Moneron, G., Nusser, Z., & DiGregorio, D. A. (2019). Distinct Nanoscale Calcium Channel and Synaptic Vesicle Topographies Contribute to the Diversity of Synaptic Function. *Neuron*, *104*(4), 693-710.e9. https://doi.org/10.1016/j.neuron.2019.08.014

Reijntjes, D. O. J., Köppl, C., & Pyott, S. J. (2020). Volume gradients in inner hair cell-auditory nerve fiber pre- and postsynaptic proteins differ across mouse strains. *Hearing Research*, *390*, 107933. https://doi.org/10.1016/j.heares.2020.107933

Reijntjes, D. O. J., & Pyott, S. J. (2016). The afferent signaling complex: Regulation of type I spiral ganglion neuron responses in the auditory periphery. *Hearing Research*, *336*, 1–16. https://doi.org/10.1016/j.heares.2016.03.011

Relkin, E. M., & Doucet, J. R. (1991). Recovery from prior stimulation. I: Relationship to spontaneous firing rates of primary auditory neurons. *Hearing Research*, *55*(2), 215–222.

Rhode, W. S., & Smith, P. H. (1985). Characteristics of tone-pip response patterns in relationship to spontaneous rate in cat auditory nerve fibers. *Hearing Research*, *18*(2), 159–168.

Robertson, D., & Paki, B. (2002). Role of L-Type Ca2+ Channels in Transmitter Release From Mammalian Inner Hair Cells. II. Single-Neuron Activity. *Journal of Neurophysiology*, *87*(6), 2734–2740.

Romand, R. (1984). Functional properties of auditory-nerve fibers during postnatal development in the kitten. *Experimental Brain Research*, *56*(3), 395–402.

Rosenmund, C., Sigler, A., Augustin, I., Reim, K., Brose, N., & Rhee, J. S. (2002). Differential control of vesicle priming and short-term plasticity by Munc13 isoforms. *Neuron*, *33*(3), 411–424. https://doi.org/10.1016/S0896-6273(02)00568-8

Ruel, J., Nouvian, R., D'Aldin, C. G., Pujol, R., Eybalin, M., & Puel, J.-L. (2001). Dopamine inhibition of auditory nerve activity in the adult mammalian cochlea. *European Journal of Neuroscience*, *14*(6), 977–986. https://doi.org/10.1046/j.0953-816x.2001.01721.x

Russell, I. J., & Sellick, P. M. (1978). Intracellular studies of hair cells in the mammalian cochlea. *The Journal of Physiology*, *284*, 261–290.

Rutherford, M. A., Chapochnikov, N. M., & Moser, T. (2012). Spike Encoding of Neurotransmitter Release Timing by Spiral Ganglion Neurons of the Cochlea. *The Journal of Neuroscience*, *32*(14), 4773–4789. https://doi.org/10.1523/JNEUROSCI.4511-11.2012

Sachs, M. B., & Abbas, P. J. (1974). Rate versus level functions for auditory-nerve fibers in cats: Tone-burst stimuli. *The Journal of the Acoustical Society of America*, *56*(6), 1835–1847. https://doi.org/10.1121/1.1903521

Sachs, M. B., Winslow, R. L., & Sokolowski, B. H. (1989). A computational model for rate-level functions from cat auditory-nerve fibers. *Hearing Research*, *41*(1), 61–69. https://doi.org/10.1016/0378-5955(89)90179-2

Schmiedt, R. A. (1989). Spontaneous rates, thresholds and tuning of auditory-nerve fibers in the gerbil: Comparisons to cat data. *Hearing Research*, *42*(1), 23–35.

Schnee, M. E., Castellano-Muñoz, M., & Ricci, A. J. (2013). Response properties from turtle auditory hair cell afferent fibers suggest spike generation is driven by synchronized release both between and within synapses. *Journal of Neurophysiology*, *110*(1), 204–220. https://doi.org/10.1152/jn.00121.2013

Schnee, M. E., Lawton, D. M., Furness, D. N., Benke, T. A., & Ricci, A. J. (2005). Auditory hair cell-afferent fiber synapses are specialized to operate at their best frequencies. *Neuron*, *47*(2), 243–254. https://doi.org/10.1016/j.neuron.2005.06.004

Schnee, M. E., Santos-Sacchi, J., Castellano-Muñoz, M., Kong, J.-H., & Ricci, A. J. (2011). Calcium-Dependent Synaptic Vesicle Trafficking Underlies Indefatigable Release at the Hair Cell Afferent Fiber Synapse. *Neuron*, *70*(2), 326–338. https://doi.org/10.1016/j.neuron.2011.01.031

Schroeder, M. R., & Hall, J. L. (1974). Model for mechanical to neural transduction in the auditory receptor. *The Journal of the Acoustical Society of America*, *55*(5), 1055–1060.

Scimemi, A., & Diamond, J. S. (2012). The number and organization of Ca2+ channels in the active zone shapes neurotransmitter release from Schaffer collateral synapses. *The Journal of Neuroscience: The Official Journal of the Society for Neuroscience*, *32*(50), 18157–18176. https://doi.org/10.1523/JNEUROSCI.3827-12.2012

Sheng, J., He, L., Zheng, H., Xue, L., Luo, F., Shin, W., Sun, T., Kuner, T., Yue, D. T., & Wu, L.-G. (2012). Calcium-channel number critically influences synaptic strength and plasticity at the active zone. *Nature Neuroscience*, *15*(7), 998–1006. https://doi.org/10.1038/nn.3129

Shin, W., Arpino, G., Thiyagarajan, S., Su, R., Ge, L., McDargh, Z., Guo, X., Wei, L., Shupliakov, O., Jin, A., O'Shaughnessy, B., & Wu, L.-G. (2020). Vesicle Shrinking and Enlargement Play Opposing Roles in the Release of Exocytotic Contents. *Cell Reports*, *30*(2), 421-431.e7. https://doi.org/10.1016/j.celrep.2019.12.044

Shin, W., Ge, L., Arpino, G., Villarreal, S. A., Hamid, E., Liu, H., Zhao, W.-D., Wen, P. J., Chiang, H.-C., & Wu, L.-G. (2018). Visualization of Membrane Pore in Live Cells Reveals a Dynamic-

Pore Theory Governing Fusion and Endocytosis. *Cell*, *173*(4), 934-945.e12. https://doi.org/10.1016/j.cell.2018.02.062

Shrestha, B. R., Chia, C., Wu, L., Kujawa, S. G., Liberman, M. C., & Goodrich, L. V. (2018). Sensory Neuron Diversity in the Inner Ear Is Shaped by Activity. *Cell*, *174*(5), 1229-1246.e17. https://doi.org/10.1016/j.cell.2018.07.007

Smith, K. E., Browne, L., Selwood, D. L., McAlpine, D., & Jagger, D. J. (2015). Phosphoinositide Modulation of Heteromeric Kv1 Channels Adjusts Output of Spiral Ganglion Neurons from Hearing Mice. *Journal of Neuroscience*, *35*(32), 11221–11232. https://doi.org/10.1523/JNEUROSCI.0496-15.2015

Spassova, M. A., Avissar, M., Furman, A. C., Crumling, M. A., Saunders, J. C., & Parsons, T. D. (2004). Evidence that rapid vesicle replenishment of the synaptic ribbon mediates recovery from short-term adaptation at the hair cell afferent synapse. *Journal of the Association for Research in Otolaryngology: JARO*, *5*(4), 376–390.

Sun, S., Babola, T., Pregernig, G., So, K. S., Nguyen, M., Su, S.-S. M., Palermo, A. T., Bergles, D. E., Burns, J. C., & Müller, U. (2018). Hair Cell Mechanotransduction Regulates Spontaneous Activity and Spiral Ganglion Subtype Specification in the Auditory System. *Cell*, *174*(5), 1247-1263.e15. https://doi.org/10.1016/j.cell.2018.07.008

Taberner, A. M., & Liberman, M. C. (2005). Response Properties of Single Auditory Nerve Fibers in the Mouse. *Journal of Neurophysiology*, *93*(1), 557–569. https://doi.org/10.1152/jn.00574.2004

Tsuji, J., & Liberman, M. C. (1997). Intracellular labeling of auditory nerve fibers in guinea pig: Central and peripheral projections. *The Journal of Comparative Neurology*, *381*(2), 188–202.

Vogl, C., Cooper, B. H., Neef, J., Wojcik, S. M., Reim, K., Reisinger, E., Brose, N., Rhee, J.-S., Moser, T., & Wichmann, C. (2015). Unconventional molecular regulation of synaptic vesicle replenishment in cochlear inner hair cells. *Journal of Cell Science*, *128*(4), 638–644. https://doi.org/10.1242/jcs.162099

Walsh, E. J., & McGee, J. (1987). Postnatal development of auditory nerve and cochlear nucleus neuronal responses in kittens. *Hearing Research*, *28*(1), 97–116. https://doi.org/16/0378-5955(87)90157-2

Wangemann, P., & Schacht, J. (1996). Homeostatic Mechanisms in the Cochlea. In P. Dallos, A. N. Popper, & R. R. Fay (Eds.), *The Cochlea* (pp. 130–185). Springer New York. https://doi.org/10.1007/978-1-4612-0757-3_3

Wichmann, C., & Kuner, T. (2022). Heterogeneity of glutamatergic synapses: Cellular mechanisms and network consequences. *Physiological Reviews*, *102*(1), 269–318. https://doi.org/10.1152/physrev.00039.2020

Winter, I. M., Robertson, D., & Yates, G. K. (1990). Diversity of characteristic frequency rate-intensity functions in guinea pig auditory nerve fibres. *Hearing Research*, *45*(3), 191–202. https://doi.org/10.1016/0378-5955(90)90120-E

Wong, A. B., Jing, Z., Rutherford, M. A., Frank, T., Strenzke, N., & Moser, T. (2013). Concurrent Maturation of Inner Hair Cell Synaptic Ca2+ Influx and Auditory Nerve Spontaneous Activity around Hearing Onset in Mice. *The Journal of Neuroscience*, *33*(26), 10661–10666. https://doi.org/10.1523/JNEUROSCI.1215-13.2013

Wu, J. S., Yi, E., Manca, M., Javaid, H., Lauer, A. M., & Glowatzki, E. (2020). Sound exposure dynamically induces dopamine synthesis in cholinergic LOC efferents for feedback to auditory nerve fibers. *ELife*, *9*, e52419. https://doi.org/10.7554/eLife.52419

Wu, J. S., Young, E. D., & Glowatzki, E. (2016). Maturation of Spontaneous Firing Properties after Hearing Onset in Rat Auditory Nerve Fibers: Spontaneous Rates, Refractoriness, and Interfiber Correlations. *Journal of Neuroscience*, *36*(41), 10584–10597. https://doi.org/10.1523/JNEUROSCI.1187-16.2016

Xu, W., & Lipscombe, D. (2001). Neuronal CaV1.3α1 L-Type Channels Activate at Relatively Hyperpolarized Membrane Potentials and Are Incompletely Inhibited by Dihydropyridines. *The Journal of Neuroscience*, *21*(16), 5944–5951.

Yang, Y.-M., Fedchyshyn, M. J., Grande, G., Aitoubah, J., Tsang, C. W., Xie, H., Ackerley, C. A., Trimble, W. S., & Wang, L.-Y. (2010). Septins regulate developmental switching from microdomain to nanodomain coupling of Ca2+ influx to neurotransmitter release at a central synapse. *Neuron*, *67*(1), 100–115. https://doi.org/10.1016/j.neuron.2010.06.003

Yates, G. K., Winter, I. M., & Robertson, D. (1990). Basilar membrane nonlinearity determines auditory nerve rate-intensity functions and cochlear dynamic range. *Hearing Research*, *45*(3), 203–219.

Yin, Y., Liberman, L. D., Maison, S. F., & Liberman, M. C. (2014). Olivocochlear innervation maintains the normal modiolar-pillar and habenular-cuticular gradients in cochlear synaptic morphology. *Journal of the Association for Research in Otolaryngology: JARO*, *15*(4), 571–583. https://doi.org/10.1007/s10162-014-0462-z

Young, E. D., Wu 武靜靜, J. S., Niwa, M., & Glowatzki, E. (2021). Resolution of subcomponents of synaptic release from postsynaptic currents in rat hair-cell/auditory-nerve fiber synapses. *Journal of Neurophysiology*, *125*(6), 2444–2460. https://doi.org/10.1152/jn.00450.2020